



Dynamically coupled kinetic chemistry in brown dwarf atmospheres – I. Performing global scale kinetic modelling

Elsbeth K. H. Lee ¹★, Xianyu Tan ^{2,3} and Shang-Min Tsai⁴

¹Center for Space and Habitability, University of Bern, Gesellschaftsstrasse 6, CH-3012 Bern, Switzerland

²Tsung-Dao Lee Institute, Shanghai Jiao Tong University, 520 Shengrong Road, Shanghai 201210, China

³School of Physics and Astronomy, Shanghai Jiao Tong University, 800 Dongchuan Road, Shanghai 200240, China

⁴Department of Earth Sciences, University of California, 900 University Ave, Riverside, CA 92521, USA

Accepted 2023 June 5. Received 2023 May 25; in original form 2023 April 20

ABSTRACT

The atmospheres of brown dwarfs have been long observed to exhibit a multitude of non-equilibrium chemical signatures and spectral variability across the L, T, and Y spectral types. We aim to investigate the link between the large-scale 3D atmospheric dynamics and time-dependent chemistry in the brown dwarf regime, and to assess its impact on spectral variability. We couple the miniature kinetic chemistry module ‘MINI-CHEM’ to the EXO-FMS general circulation model (GCM). We then perform a series of idealized brown dwarf regime atmospheric models to investigate the dynamical 3D chemical structures produced by our simulations. The GCM output is post-processed using a 3D radiative transfer model to investigate hemisphere-dependent spectral signatures and rotational variability. Our results show the expected strong non-equilibrium chemical behaviour brought on by vertical mixing and global spatial variations due to zonal flows. Chemical species are generally globally homogenized, showing variations of ± 10 per cent or less, dependent on pressure level, and follow the dynamical structures present in the atmosphere. However, we find localized storm regions and eddies can show higher contrasts, up to ± 100 per cent, in mixing ratio compared to the background global mean. This initial study represents another step in understanding the connection between 3D atmospheric flows in brown dwarfs and their rich chemical inventories.

Key words: hydrodynamics – methods: numerical – planets and satellites: atmospheres – planets and satellites: gaseous planets – stars: atmospheres – brown dwarfs.

1 INTRODUCTION

The study of chemical non-equilibrium processes in brown dwarf atmospheres has been an important factor in explaining their observed spectral features. Several groups of molecules and their non-equilibrium properties have been examined in detail in the literature, in particular, CH_4 – CO , NH_3 – N_2 – HCN , and CO_2 . Observed spectral feature strengths of each species group vary with the effective temperature and gravity of the brown dwarfs.

L dwarfs are within the effective temperature range of $T_{\text{eff}} \approx 2200$ – 1400 K. Generally, L dwarfs are characterized by their strong optical wavelength absorbers in their atmosphere such as Na, K and hydrides such as CaH and FeH, although the dominant absorbing species varies greatly with spectral subtype. The strong TiO and VO bands seen in M dwarf spectra are weakened substantially in L dwarf spectra. The most prominent infrared molecular features are H_2O and CO, found across the whole spectral type.

T dwarfs are within the effective temperature range of $T_{\text{eff}} \approx 1400$ – 500 K, characterized spectroscopically with the onset of stronger CH_4 absorption features (e.g. Burgasser et al. 2002a). The early-T objects tend to better fit with cloudless or very thin cloud deck atmospheric models (e.g. Marley et al. 1996; Burgasser et al. 2002b), suggesting

the refractory clouds found in the L dwarf regime have been removed from the upper atmosphere. However, models with minor clouds can also explain the spectrum of these objects well, in particular the later-T objects (e.g. Morley et al. 2012). The condensation of refractory elements removes the strong optical absorbers such as TiO, VO, and Fe from the photospheric regions. In the infrared, stronger CH_4 features appear and begin to dominate the spectrum compared to CO. However, hints of CO can still appear in the spectra of late T-dwarfs, suggesting their atmospheres are in chemical non-equilibrium (e.g. Geballe et al. 2009). For example, the well-studied T brown dwarf Gliese 229B ($T_{\text{eff}} \approx 900$ K) shows clear signals of CO absorption in the atmosphere (e.g. Noll, Geballe & Marley 1997; Oppenheimer et al. 1998; Saumon et al. 2000). Calamari et al. (2022) were able to constrain the amount of CO on Gliese 229B using a retrieval model, and find a T_{eff} of the brown dwarf around 100 K smaller than the spectral energy distribution (SED)-derived value. Recently, Miles et al. (2023) published a highly detailed spectrum of VHS 1256 b, which is a red, low gravity L–T transition-type object, across the full infrared wavelength regime using a plethora of instruments onboard *JWST*. They found evidence of disequilibrium chemistry from the strength of the CH_4 spectral absorption features and a multitude of other species at non-equilibrium abundances.

Y dwarfs are brown dwarfs that have cooled to $T_{\text{eff}} \lesssim 500$ K at this stage in their evolution. These are dominated by CH_4 absorption and, due to their colder temperatures, have the possibility to contain water

* E-mail: elsbeth.lee@csh.unibe.ch

(e.g. Morley et al. 2018; Mang et al. 2022; Lacy & Burrows 2023) or KCl (e.g. Mang et al. 2022) clouds, which makes them interesting analogues to our own Solar system objects and more temperate climate objects. Observational studies of late-T and Y brown dwarfs have also invoked chemical non-equilibrium processes in order to explain spectral feature strengths. For example, in recent studies, Miles et al. (2020) perform M-band spectroscopy on a selection of late-T and Y dwarfs ($T_{\text{eff}} \approx 750\text{--}250$ K). They find evidence of increased CO absorption across all their objects, not expected to be present when assuming chemical equilibrium. They attempt to derive the eddy diffusion parameter, K_{zz} , and CO quench levels from their observed spectral features. Leggett et al. (2021) also showed the importance of taking non-equilibrium into account when fitting data to models. They find a modified deep adiabat with CO and NH_3 in non-equilibrium can better fit the observed data trends in their Y-dwarf sample.

In the irradiated exoplanet regime, non-equilibrium chemistry is also expected, with photochemical processes also impacting the chemical structure of the atmosphere, with a recent example being the discovery and characterization of SO_2 on WASP-39 b using *JWST* instruments (Alderson et al. 2023; Rustamkulov et al. 2023; Tsai et al. 2023). In 3D, Drummond et al. (2020) and Zamyatina et al. (2023) couple the Venot et al. (2019) thermochemical kinetic network to the UK Met Office Unified Model general circulation model (GCM; Mayne et al. 2014). They focused on the canonical hot Jupiter exoplanets HD 209458 b, HD 189733 b, HAT-P-11 b, and WASP-17 b. They found all the planets showed vertical and zonal/meridional quenching with strong homogenization of chemical species across the globe. Their HD 189733 b simulation exhibited the most observable transport-induced quenching behaviour. These 3D studies on hot Jupiter atmospheres are highly complementary to this study on brown dwarf atmospheres.

Overall, the major theme of the above and many more observational studies of brown dwarfs in the literature is the invocation of non-equilibrium chemical processes as an explanation for their observed spectral properties, in particular the minor species spectral features in the infrared. In this study, we explore the 3D non-equilibrium chemistry of brown dwarf atmospheres by performing idealized simulations that couple a miniature kinetic chemistry module, MINI-CHEM, to the EXO-FMS 3D GCM. We perform five simulations across the effective temperature range: $T_{\text{eff}} = 500, 750, 1000, 1250, \text{ and } 1500$ K.

In Section 2, we summarize approaches to modelling brown dwarf atmospheric chemistry. In Sections 3 and 4, we summarize the MINI-CHEM kinetic chemistry module and the EXO-FMS GCM set-up for the brown dwarf simulations. In Section 5, we present the dynamical properties of each simulations. In Section 6, we present the 3D chemical properties and spatial distribution of the coupled model from simulation. In Section 7, we present spectra of our simulation outputs, examining the equator and pole differences and rotational variation. Section 8 contains a discussion of our results. Section 9 contains the summary and conclusions of our study.

2 APPROACHES TO BROWN DWARF ATMOSPHERIC CHEMISTRY

The modelling of brown dwarf atmospheres has a large and expansive history (e.g. see Helling & Casewell 2014; Marley & Robinson 2015; Zhang 2020, for comprehensive reviews). Most brown dwarf atmospheres to date have applied some version of chemical equilibrium assumption into their construction (e.g. Allard et al. 2001; Allard, Homeier & Freytag 2011; Morley et al. 2012, 2014; Saumon et al.

2012; Phillips et al. 2020). Some models have included cloud models of various flavours, linked to equilibrium condensation for example, applying a ‘rainout’ method where condensed elements are removed from the gas phase at pressures lower than their condensation pressure (e.g. Marley et al. 2002, 2021). Others have directly coupled cloud formation models such as the Ackerman & Marley (2001) EDDYSED model (e.g. Stephens et al. 2009; Morley et al. 2012) and the kinetic cloud formation model DRIFT (e.g. Helling, Woitke & Thi 2008) in the case of the DRIFT-PHOENIX models (Witte, Helling & Hauschildt 2009). These models also account for the removal of elements from the gas phase due to the cloud formation process.

A common practice in the literature to include the effects of non-equilibrium chemistry is to derive chemical time-scales from a limiting (typically slow) reaction step that sets the quench level of a species. This was first proposed for Jupiter by Prinn & Barshay (1977) to explain the detectable CO abundance in its atmosphere. Fegley & Lodders (1996) then suggested similar processes to occur in brown dwarf atmospheres. This technique or similar time-scale analysis has been applied in several studies to estimate departures from chemical equilibrium in brown dwarf 1D atmospheric models (e.g. Hubeny & Burrows 2007; Phillips et al. 2020; Karalidi et al. 2021; Mukherjee et al. 2022; Lacy & Burrows 2023).

Visscher & Moses (2011) perform 1D chemical kinetics models of Gliese 229B and HD 189733 b examining in detail the quench levels of CO and CH_4 and the dependence on the strength of K_{zz} on the mixing ratio of the quenched species in the mid-upper atmosphere. Zahnle & Marley (2014) use a full 1D chemical kinetics model to explore a range of atmospheric parameters, from $T_{\text{eff}} = 500\text{--}1100$ K, $K_{\text{zz}} = 10^4\text{--}10^{11} \text{ cm}^2 \text{ s}^{-1}$, and $\log g = 3\text{--}5 \text{ cm s}^{-2}$. They focus on the finding quench points of key molecules such as CH_4 , CO, NH_3 , N_2 , HCN, and CO_2 and the accuracy and derivation of simple expressions for the quench points through analysis of chemical time-scales. These time-scales have been extensively used for 1D atmospheric models.

3D approaches investigating chemical kinetics in this regime have been scarce in the literature. Bordwell, Brown & Oishi (2018) perform 2D and 3D modelling of small-scale convection and mixing in brown dwarf and exoplanet regimes. They include a reactive tracer coupled to the flow to investigate the connection between parametrizations of 1D diffusion approximations (through the use of the K_{zz} eddy diffusion parameter) and the 2D/3D small-scale flows in the convective zone of the atmosphere.

3 MINI-CHEM

MINI-CHEM is an open source¹ miniature chemical kinetics solver for gas giant atmospheres, described in Tsai, Lee & Pierrehumbert (2022) and Lee et al. (2023), developed as an offshoot of the VULCAN 1D chemical kinetics model (Tsai et al. 2017, 2021). In Lee et al. (2023), the thermochemistry of WASP-39 b and HD 189733 b was explored in 3D by coupling MINI-CHEM to the EXO-FMS GCM model. MINI-CHEM utilizes ‘net forward rate’ reaction tables, which greatly reduces the number of species and reactions (12 and 10, respectively, for the C–H–N–O scheme) compared to other reduced kinetic schemes, for example, the Venot et al. (2019) network used in Drummond et al. (2020) contains 30 species with 181 reactions. This comes at the cost of some accuracy and an assumption of a metallicity when constructing the net reaction tables (Tsai et al. 2022), but retains the classic chemical kinetic solver methodology. Currently,

¹https://github.com/ELeeAstro/mini_chem

Table 1. Adopted EXO-FMS GCM simulation parameters for the brown dwarf atmosphere simulations. We use a cubed-sphere resolution of C96 ($\approx 384 \times 192$ in longitude \times latitude).

Symbol	Value	Unit	Description
T_{eff}	500, 750, 1000 1250, 1500	K	Effective temperature
P_0	100	bar	Reference surface pressure
P_{up}	10^{-4}	bar	Upper boundary pressure
P_{rcb}	10	bar	Radiative convective boundary
c_p	13 000	$\text{J K}^{-1} \text{kg}^{-1}$	Specific heat capacity
R	3714	$\text{J K}^{-1} \text{kg}^{-1}$	Ideal gas constant
κ	0.286	–	Adiabatic coefficient
g_{bd}	1000	m s^{-2}	Acceleration from gravity
R_{bd}	7.149×10^7	m	Radius of brown dwarf
Ω_{bd}	1.745×10^{-4}	rad s^{-1}	Rotation rate of brown dwarf
M/H	0	–	\log_{10} solar metallicity
T_{amp}	1.03×10^{-5} , 8.39×10^{-5} , 3.71×10^{-4} 1.2×10^{-3} , 3.0×10^{-3}	K s^{-1}	Perturbation temperature amplitude
τ_{storm}	10^5	s	Storm time-scale
Δt_{hyd}	60	s	Hydrodynamic time-step
Δt_{rad}	60	s	Radiative time-step
Δt_{ch}	3600	s	MINI-CHEM time-step
N_v	60	–	Vertical resolution
d_4	0.16	–	$\mathcal{O}(4)$ divergence dampening coefficient

the scheme only includes thermochemistry without photochemical reactions.

We include helium as a passive, inert, chemical tracer that is evolved with the flow and contributes to the total volume mixing ratio (VMR), but does not alter any of the reacting species inside MINI-CHEM. We integrate MINI-CHEM every hour of simulation time, for a chemical time-step of $\tau_{\text{chem}} = 3600$ s. This allows a good compromise between computational efficiency and time-dependent accuracy. We use the SEULEX² stiff ordinary differential equation (ODE) solver to integrate the network in time.

4 GCM MODELLING

Overall, we follow a similar general circulation model (GCM) set-up to the isolated brown dwarf MITGCM modelling efforts of Showman, Tan & Zhang (2019), Tan & Showman (2021b), and Tan (2022), adapted to the EXO-FMS GCM framework. EXO-FMS has been used to study terrestrial planets (Hammond & Pierrehumbert 2017), gas giant atmospheres (Lee et al. 2021), warm Neptunes (Innes & Pierrehumbert 2022), and irradiated brown dwarfs orbiting white dwarfs (Lee et al. 2020). It is therefore well suited to perform the current suite of brown dwarf atmospheric simulations. Table 1 shows the GCM parameters used for each simulation.

We use a two-stream short characteristics method with Bézier interpolants (e.g. de la Cruz Rodríguez & Piskunov 2013) to calculate the vertical thermal radiation flux. For the gas-phase opacity we follow the same scheme as in Tan (2022), using the Freedman et al. (2014) Rosseland mean opacity fitting function with a minimum opacity of $\kappa_{\text{gas}} = 10^{-3} \text{ m}^2 \text{ kg}^{-1}$. This grey limit is required to stabilize the scheme in the low optical depth limit, where the Rosseland mean is not as accurate at representing the atmospheric opacity and a Planck mean should be preferred (e.g. Heng 2017). This method does not include scattering, however, significant thermal scattering

is only expected in the presence of cloud particles, not applicable to the cloud-free models in this study.

We include the vertical convective transport of chemical tracers in-line with the dry convective adjustment scheme. This mixes chemical species in a way parallel to the temperature changes when the dry convection adjustment is triggered by homogenizing the VMR of species between vertical layers that undergo adjustment. As in the temperature adjustment, the scheme is performed until the vertical temperature–pressure profile is stable to convection. This operates instantaneously, the same way as the temperature adjustment is performed in the convective adjustment scheme. As a result, chemical tracers are highly efficiently mixed inside the adiabatic region as expected from smaller scale simulations in similar regimes (e.g. Freytag et al. 2010; Bordwell et al. 2018). We note the GCM model cannot resolve individual convective plumes that would be much smaller than the grid resolution used here.

In addition, we also note that different approaches to tracer mixing in convective regions exist such as mixing length theory (e.g. see Marley & Robinson 2015). Using mixing length theory would allow tracers to mix through the calculation of an eddy diffusion coefficient, K_{zz} , derived from the convective heat flux. However, in this study, we retain the convective adjustment scheme as it is simpler to implement inside the GCM framework. Examining the differences between a mixing length theory approach and convective adjustment inside the GCM is left to future studies.

To induce a dynamical response in the atmosphere we follow the thermal perturbation forcing scheme used in previous brown dwarf dynamics studies (Showman et al. 2019; Lian et al. 2022; Tan 2022). This scheme aims to approximate the perturbations induced through convective plume motions from deeper in the atmosphere. The term ‘forcing’ in the context of atmospheric dynamical modelling generally refers to the way the sources of thermodynamic heating and cooling or angular momentum are implemented to drive the atmospheric flow. We follow directly the vertical perturbation form in Tan (2022), choosing a constant radiative–convective boundary pressure of 10 bar for each simulation and storm time-scale, τ_{storm} , of 10^5 s. The thermal perturbation amplitude is changed dependent

²<https://www.unige.ch/~hairer/software.html>

on the effective temperature (Table 1), which is calculated following the approximations found in Showman et al. (2019). Without this perturbation scheme, the atmosphere remains static in radiative–convective equilibrium without the involvement of the atmospheric wind structure.

We apply a deep ‘linear basal drag’, implemented as a Rayleigh drag term as in Tan & Showman (2021b), using a surface drag at the lower boundary (100 bar) that is linearly decreased in strength to a pressure of 50 bar. This emulates a moderate deep drag from magnetic and other drag sources on the atmosphere (e.g. Beltz et al. 2022). Such schemes are commonly used in gas giant planet atmospheric simulations (e.g. Liu & Showman 2013; Komacek & Showman 2016; Carone et al. 2020). We chose a ‘middle ground’ drag time-scale of $\tau_{\text{drag}} = 10^6$ s to allow larger scale dynamical features to develop, compared to the more dampened dynamics exhibited by smaller drag time-scales (Tan 2022). Other drag time-scale values, 10^5 and 10^7 s, were explored in Tan & Showman (2021b) and Tan (2022), and its impact on the atmospheric dynamics was assessed. Kinetic energy removed through this deep Rayleigh drag is returned to the atmosphere as localized increases in thermal energy.

Rotation periods of brown dwarfs span from about 1 h to nearly 20 h according to spectroscopic and photometric observations (e.g. Reiners & Basri 2008; Metchev et al. 2015; Tannock et al. 2021). We chose a rotation period of 10 h as a representative value in this work, following a middle ground value from the Tan & Showman (2021b) suite of brown dwarf models. A higher rotation rate typically results in smaller scale horizontal dynamical features, requiring a greater horizontal resolution in the GCM to adequately resolve. Our assumed moderate rotation period allows us to avoid using a higher GCM grid resolution than C96, required for accurate capture of smaller scale features that appear at such a rotation period while retaining strong rotationally driven flows. Increasing the rotation rate and resolution of the GCM would require a large boost in available computational power to perform.

With a drag time-scale of 10^6 s, the atmosphere achieves statistical equilibrium after around 1000 d of simulation (Tan 2022). All GCM models are therefore run for 1000 simulated days before coupling to MINI-CHEM is included. We assume chemical equilibrium as the VMR initial conditions for each species in the atmosphere starting at 1000 d, after which MINI-CHEM is used to evolve the VMR composition of the atmosphere. During testing, it was found that the kinetics solver was too slow with integrating high-pressure, high-temperature deep atmospheric regions where the chemical time-scales are very small, with the exception of the $T_{\text{eff}} = 500$ K and, surprisingly, the $T_{\text{eff}} = 1500$ K model. We therefore enforce chemical equilibrium for pressure levels greater than ≈ 20 bar in the 750, 1000, and 1250 K models to ensure a smooth VMR profile and expedient computational completion time.

We run the coupled scheme until 2100 d for the $T_{\text{eff}} = 500, 750$, and 1000 K simulations and 1900 and 1400 d for the $T_{\text{eff}} = 1250$ and 1500 K models, respectively. We find that the $T_{\text{eff}} = 1250$ and 1500 K models converge faster compared to the cooler models due to being forced with a larger temperature perturbation amplitude.

5 3D DYNAMICAL STRUCTURES

In this section, we present the dynamical structures of the five brown dwarf GCM simulations.

5.1 Zonal mean zonal velocity

In Fig. 1, we show the zonal mean zonal plots of each of the five brown dwarf GCMs. This gives an idea of the jet structures and

patterns present in each simulation. The $T_{\text{eff}} = 500$ K simulation shows evidence for a multiple alternating prograde and retrograde jet structure, typical of a fast rotator and reminiscent of Jupiter’s multiple zonal bands. The other simulations show a wide equatorial jet structure with flanking jets at latitude. This is in line with the stronger temperature perturbation amplitude zonal mean results from Tan & Showman (2021b) and Tan (2022), which show similar structures in our chosen parameter regime.

5.2 Outgoing longwave radiation

To better elucidate the energy transport and thermal structure properties at the photosphere in the simulated brown dwarf atmospheres, we present the outgoing longwave radiation (OLR) maps in Fig. 2. Here we see that each simulation exhibits different dominant dynamical structures. For example, the stronger thermal perturbation amplitude models show more ‘spottiness’ and contrasts between hotspot and coldspot. The $T_{\text{eff}} = 500$ K model shows the most obvious smaller scale dynamical patterns, with clearer delineations between jet regions. This model also shows signs of instabilities and interactions near the central jet regions.

We find in general, for the stronger amplitude forced simulations, the storm regions at higher latitudes alter the OLR patterns at the rate of the storm time-scale as expected. The dominant dynamical features such as the equatorial and at latitude jets show less variations with time, indicating that the dynamical flows provide more thermal homogeneity and stability there.

6 3D CHEMICAL STRUCTURES

In this section, we examine the resulting 3D chemical structures of the coupled MINI-CHEM GCM simulations. We present 1D global means and spatial maps of chemical species.

6.1 Global means

In Fig. 3, we present 1D globally averaged values of the temperature structure and VMR of key chemical species for each simulation, as well as the values for each species at chemical equilibrium. These figures also indicate the extent of the adiabatic region. Here it is clear each brown dwarf atmosphere exhibits strong vertical mixing that leads to the non-equilibrium behaviour of the chemical species. In particular, the strong mixing brought on by the dry convective adjustment scheme in the adiabatic regions pushes the species away from CE at the deepest parts of the atmosphere.

In Fig. 4, we show the average VMR of CO, CH₄, NH₃, and N₂ along with their minimum and maximum value ranges for each effective temperature. The trend with effective temperature of each species is seen here, with the CO–CH₄ inflection point occurring at around $T_{\text{eff}} \approx 850$ K, and the NH₃–N₂ conversion happening at $T_{\text{eff}} \approx 550$ K. Larger variations of VMR at higher effective temperatures are attributed to the stronger thermal perturbations assumed for these models, which in turn causes stronger spatial variations in the VMR of the species.

6.2 Comparison to VULCAN

In Fig. 5, we compare our global 1D mean VMR values from the GCM to 1D VMR profiles produced by VULCAN (Tsai et al. 2017, 2021) using the full C–H–N–O thermochemical network. We assume a constant eddy diffusion parameter of $K_{zz} = 10^6$ and 10^9 cm² s^{−1} for the VULCAN models, taking the global mean GCM T – p profile as the input. Differences can be seen

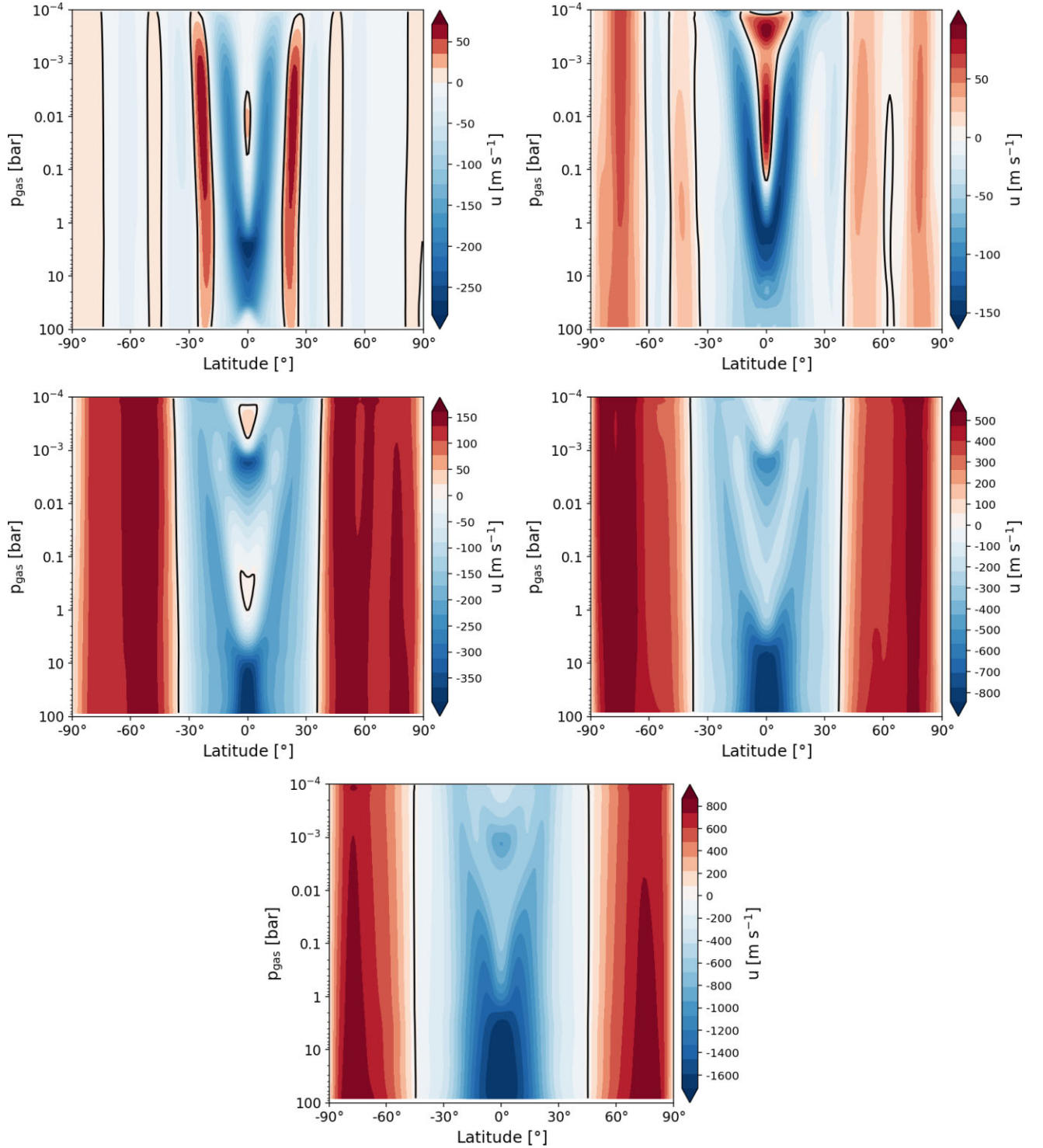


Figure 1. Zonal mean zonal velocity of each brown dwarf simulation averaged from the last 100 d of simulation. $T_{\text{eff}} = 500$ (top left), 750 (top right), 1000 (middle left), 1250 (middle right), and 1500 K (bottom). The strongest forced models (1000, 1250, and 1500 K) show large-scale jet formation patterns from the equator, with one counterrotating jet at equatorial regions, with flanking jets at higher latitudes. The cooler models (500 and 750 K) show more evidence of multiple jet structure formation.

between the 3D and 1D approaches in the quench level of some species across each effective temperature that we attribute to the K_{zz} approach used in VULCAN and the convective adjustment and large-scale dynamical mixing from advection inside the GCM.

This makes one-to-one comparison difficult, with many differences in the VMR structure, particularly in the deep regions, seen between the two approaches. This suggests that possibly simulating a deeper pressure to capture species that quench >100 bar and a time-dependent tracer mixing scheme in the adiabatic regions for

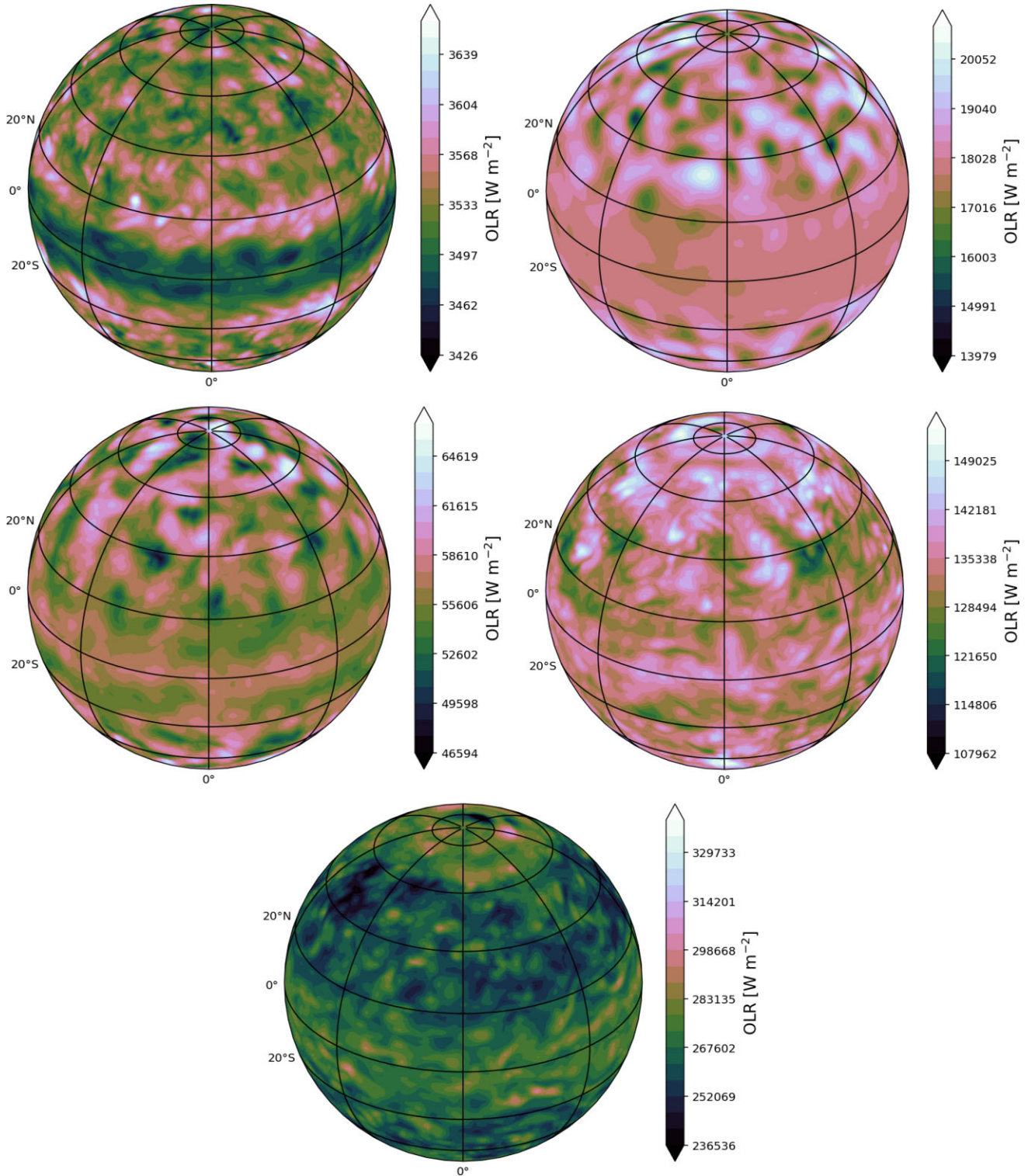


Figure 2. Outgoing longwave radiation (OLR) from each brown dwarf model at the end of the simulation. $T_{\text{eff}} = 500$ (top left), 750 (top right), 1000 (middle left), 1250 (middle right), and 1500 K (bottom). The OLR maps show the salient dynamical features that are present in the photospheric regions of the atmosphere. The photosphere in these cases is at around the 1–10 bar pressure level.

the GCM should be considerations for future modelling efforts. However, overall the 1D and 3D results generally produce consistent results, to within an order of magnitude or less for most cases, suggesting that the coupled 3D scheme produces reasonable and expected outputs, comparable to 1D full kinetics models.

6.3 Spatial variation

In Figs 6 and 7, we show the VMR spatial distribution of CH_4 and CO at a pressure level of ≈ 6 bar in each simulation. We find that generally the spatial distribution of each species follows the

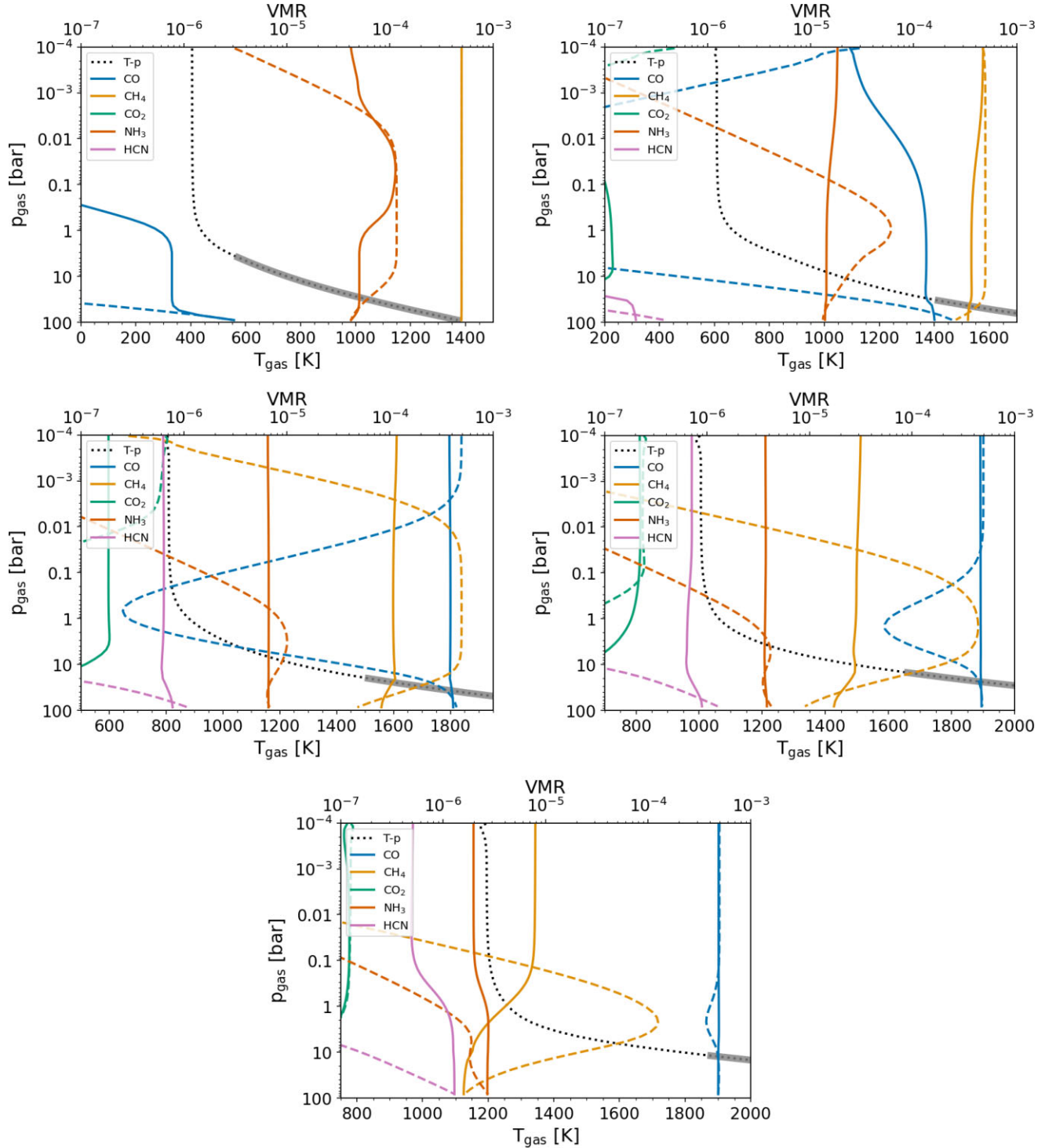


Figure 3. Global 1D mean temperature–pressure (T - p) profiles for each of the simulations (dotted black line), $T_{\text{eff}} = 500$ (top left), 750 (top right), 1000 (middle left), 1250 (middle right), and 1500 K (bottom), with the deep adiabatic region denoted by the thicker grey line. Values are taken from the average results for the last 100 d of simulation. The global 1D mean volume mixing ratios (VMRs) of various chemical species calculated with the MINI-CHEM coupled model (coloured solid lines) and assuming chemical equilibrium (coloured dashed lines) are also overplotted.

dynamical structures present in the atmosphere and is also induced by localized storm formation and dissipation. For the weaker forced and colder models ($T_{\text{eff}} = 500$ and 750 K) the VMR spatial distribution follows closely the dynamical patterns of the atmosphere, with differences between the equatorial and at latitude jet regions. Dynamical wave features at mid-latitudes are also present in the T_{eff}

$= 500$ and 750 K simulations, where the counterrotating equatorial jet and prorotating mid-latitude jet meet. Therefore, the main feature of these two models is that the global distribution of chemical species is highly dependent on the global scale dynamical properties of the atmosphere. However, the absolute range of these dynamical perturbations on the VMR of the species is very small, with a highly

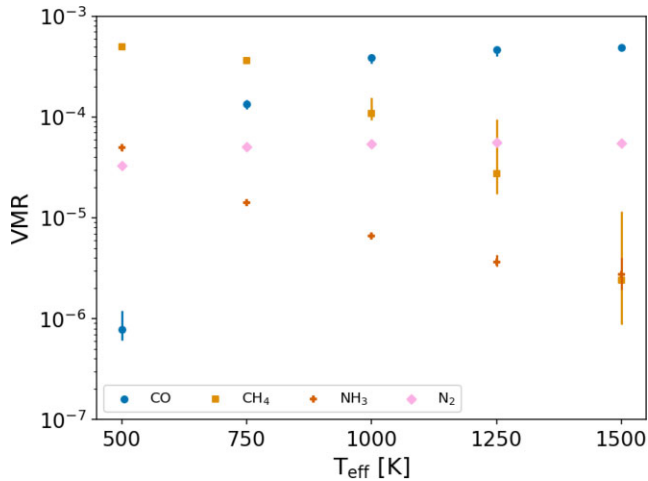


Figure 4. Mean volume mixing ratio (VMR) of different species (points) at around 6 bar for each simulation, with error bars denoting the minimum and maximum VMR range. Values are taken as a snapshot at the end of the simulation time.

homogeneous VMR, with less than 1 per cent variations, seen across the globe in these cases.

We also find that the spatial variation depends between the equator and at latitude for the hotter models ($T_{\text{eff}} = 1000, 1250, \text{ and } 1500 \text{ K}$), again following the large-scale global dynamical patterns present in the atmosphere. However, another key dynamical feature of these models is the formation and dissipation of storm regions, most strongly seen at higher latitudes. We find these local storm regions provide a significant source of spatial inhomogeneity of chemical species, either reducing or increasing the influence of a species dependent on the positive or negative temperature fluctuations in the atmosphere. These storm regions form and dissipate across a period of a given storm time-scale, the ‘severity’ and scale of the storms on the VMR of each species also depends on the amplitude of the thermal perturbation, with the stronger and hotter models showing larger VMR differences in storm regions, in line with the strength of the thermal perturbation. These storms can induce VMR variations up to around 100 per cent in local regions compared to the background mean.

Overall, we find the atmospheric spatial distributions to be non-constant and variable with time and dependent on both the global dynamical structures of the brown dwarf atmosphere and the localized temperature and dynamical changes induced by the thermal perturbation scheme. As the thermal perturbation is increased in strength, the variation in VMR within the storm regions also gets stronger.

7 EMISSION SPECTRA

We post-process the results of the brown dwarf models and produce emission spectra using the 3D radiative transfer model *gCMCRT* (Lee et al. 2022). For the gas-phase opacities, we include H_2O (Polyansky et al. 2018), CO (Li et al. 2015), CO_2 (Yurchenko et al. 2020), CH_4 (Hargreaves et al. 2020), C_2H_2 (Chubb, Tennyson & Yurchenko 2020), NH_3 (Coles, Yurchenko & Tennyson 2019), and HCN (Harris et al. 2006; Barber et al. 2014), where the line lists used to generate the opacities are the associated reference for each molecule. A correlated- k scheme is used at a resolution of $R = 100$ from 1 to $30 \mu\text{m}$, with the same Gaussian sampling scheme as Marley et al. (2021). k -tables are combined using random overlap

with resort and rebinning (e.g. Amundsen et al. 2017). $\text{H}_2\text{--H}_2$ and $\text{H}_2\text{--He}$ collisional-induced opacity is included from Karman et al. (2019). The local VMR of each species is taken directly from the coupled *MINI-CHEM* GCM output.

7.1 Field-of-view spectra

In Fig. 8, we compare the spectra at the equator and pole of each brown dwarf simulation taken as a snapshot at the last output of the simulations. Only the $T_{\text{eff}} = 1500 \text{ K}$ model shows some differences in the CH_4 bands in the near-infrared and $3.3 \mu\text{m}$ band. The rest show no appreciable difference between the spectra at the equatorial or polar regions. This result suggests that the thermal structure and chemical composition are, on average, highly similar between the equatorial regions and the poles. This is perhaps not too surprising as the thermal perturbations at the radiative–convective boundary are isotropic and there is no radiative feedback onto the thermal structure due to the changing chemical composition, which would also induce a perturbation to the temperature–pressure profile. However, including such feedback is beyond the scope of the current models at this time. We also suggest that the spatial differences in the VMR of species induced by storms at higher latitudes possibly cancel out well (at least for this one instance in time), compared to the global mean, with generally equal regions of low and high VMR of species induced by the storms.

7.2 Rotational variability and comparison to 1D models

In Fig. 9, we present spectra every hour of simulation past the end time for one rotation rate of 10 h for each of our brown dwarf models. We also take into account the rotation of the brown dwarf by calculating the emission spectrum at a longitude of $+36^\circ$ each hour. We assume an equatorial field of view of the brown dwarf, since our results in Fig. 8 suggest overall variations in latitude are minimal. This elucidates the inherent variability of the brown dwarf model due to fluctuations in temperature, dynamical features, and VMR of chemical species from the kinetic scheme across one rotational period.

Our results show that variability over one rotational period is only present in substantial quantities at near-infrared wavelengths, in the $1\text{--}1.5 \mu\text{m}$ range, and increases with larger effective temperatures. This is most likely due to these wavelengths probing the deeper regions that experience the greatest effects of the thermal perturbation scheme. The lack of variation in the mid-infrared suggests that the upper atmosphere is very stable thermally and that the spatial and time variations in VMR of species do not affect the spectrum, and storms and eddies that reduce or increase the spatial VMR tend to cancel out across the hemispheres of the brown dwarfs at these lower pressure levels.

However, we note this stability comes in part due to a lack of radiative feedback onto the thermal structure from the varying VMR structures due to using our grey radiative transfer scheme. Clouds will also affect variability significantly through impacting the thermal structure (Tan & Showman 2021b; Tan 2022), which are not included here. Inferences of storm formation and possible spots on brown dwarf atmospheres across the L and T range have been observed by several studies on brown dwarf variability (e.g. Radigan et al. 2014; Metchev et al. 2015; Apai et al. 2017; Manjavacas et al. 2019). Encouragingly, the dynamical properties of our simulations show similar spatial characteristics to the models proposed by Apai et al. (2017) to fit the variability seen in their brown dwarf sample. This suggests taking into account the thermal feedback effects will be a

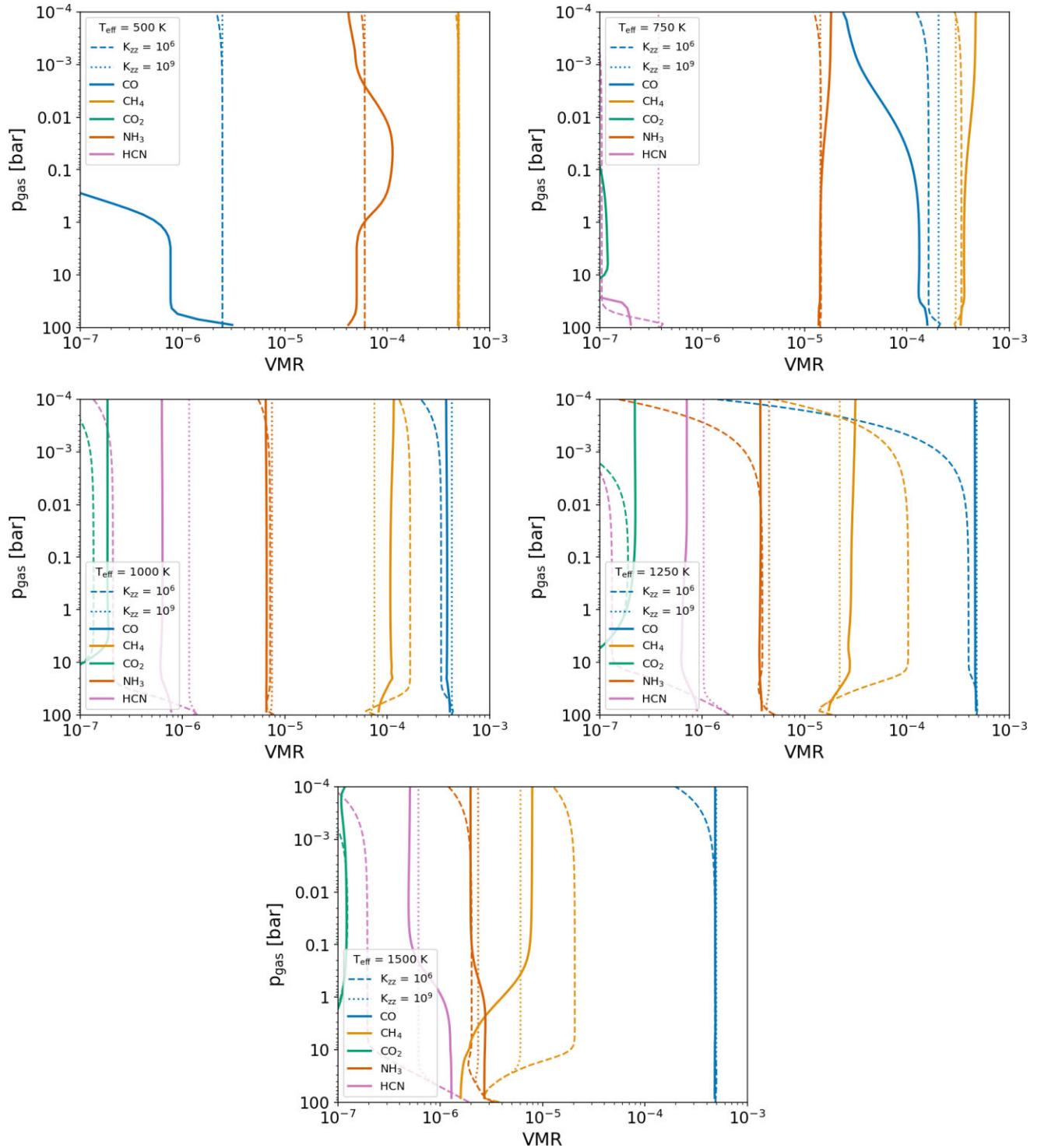


Figure 5. Global mean volume mixing ratio (VMR) profiles for each of the simulations (solid lines), $T_{\text{eff}} = 500$ (top left), 750 (top right), 1000 (middle left), 1250 (middle right), and 1500 K (bottom). Values are taken from the average results for the last 100 d of simulation. Dashed and dotted lines show the 1D VULCAN results using the full C–H–N–O kinetic network assuming a constant $K_{\text{zz}} = 10^6$ and $10^9 \text{ cm}^2 \text{ s}^{-1}$ respectively, with the global mean T – p profile used as input.

vital consideration to model the mid-infrared wavelength variability seen in brown dwarfs.

In addition, in Fig. 9, we compare the equatorial spectra of each of our brown dwarf simulations to the equivalent 1D radiative–convective equilibrium Sonora Bobcat models from Marley et al.

(2021) (i.e. the same T_{eff} , gravity, and metallicity as our GCM simulations). The Marley et al. (2021) models assume chemical equilibrium with rainout when producing the 1D T – p profiles. The output spectra from the Marley et al. (2021) are convolved to the same $R = 100$ wavelength grid used in GCMCRT.

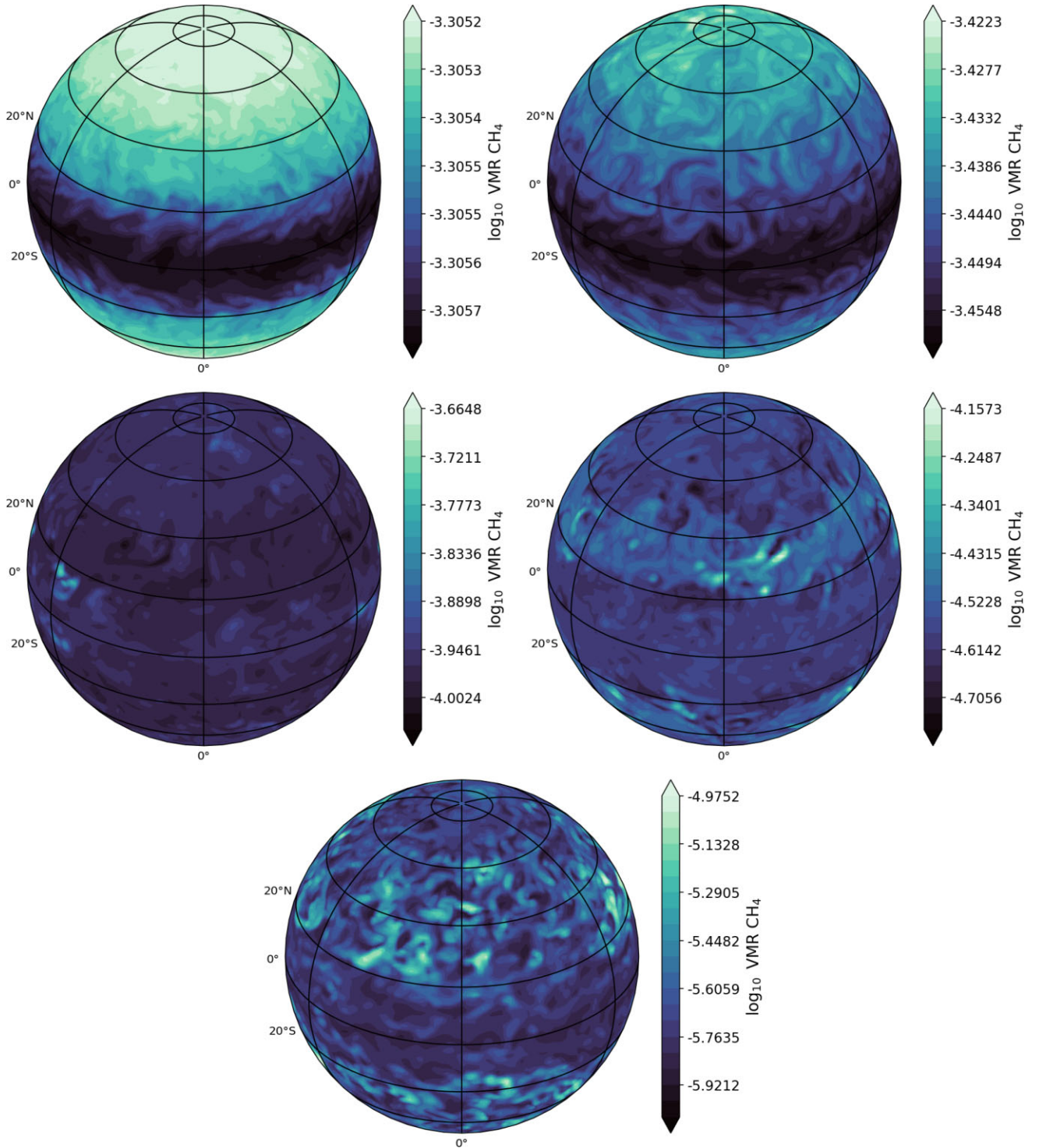


Figure 6. \log_{10} volume mixing ratio (VMR) of CH_4 (colour bar) from each brown dwarf model at the end of the simulation at around a pressure level of 6 bar. $T_{\text{eff}} = 500$ (top left), 750 (top right), 1000 (middle left), 1250 (middle right), and 1500 K (bottom). Each simulation exhibits its spatial distribution of the species dependent on the dominant dynamical feature for each parameter regime. Storm regions at higher latitudes alter the VMR of CH_4 over the course of a storm time-scale.

Our simulated spectra compare remarkably well to the Marley et al. (2021) models considering the simplified grey radiative transfer scheme used in the GCM model. However, several important differences are useful to point out. The GCM models tend to produce flatter spectra in the regions 2–4 and 5–10 μm ,

probably due to their much more isothermal upper atmospheres compared to the correlated- k scheme used in Marley et al. (2021). In addition, the GCM models generally produce a higher flux than the Marley et al. (2021) models across the infrared wavelength regime, suggesting a greater temperature present in the simulations

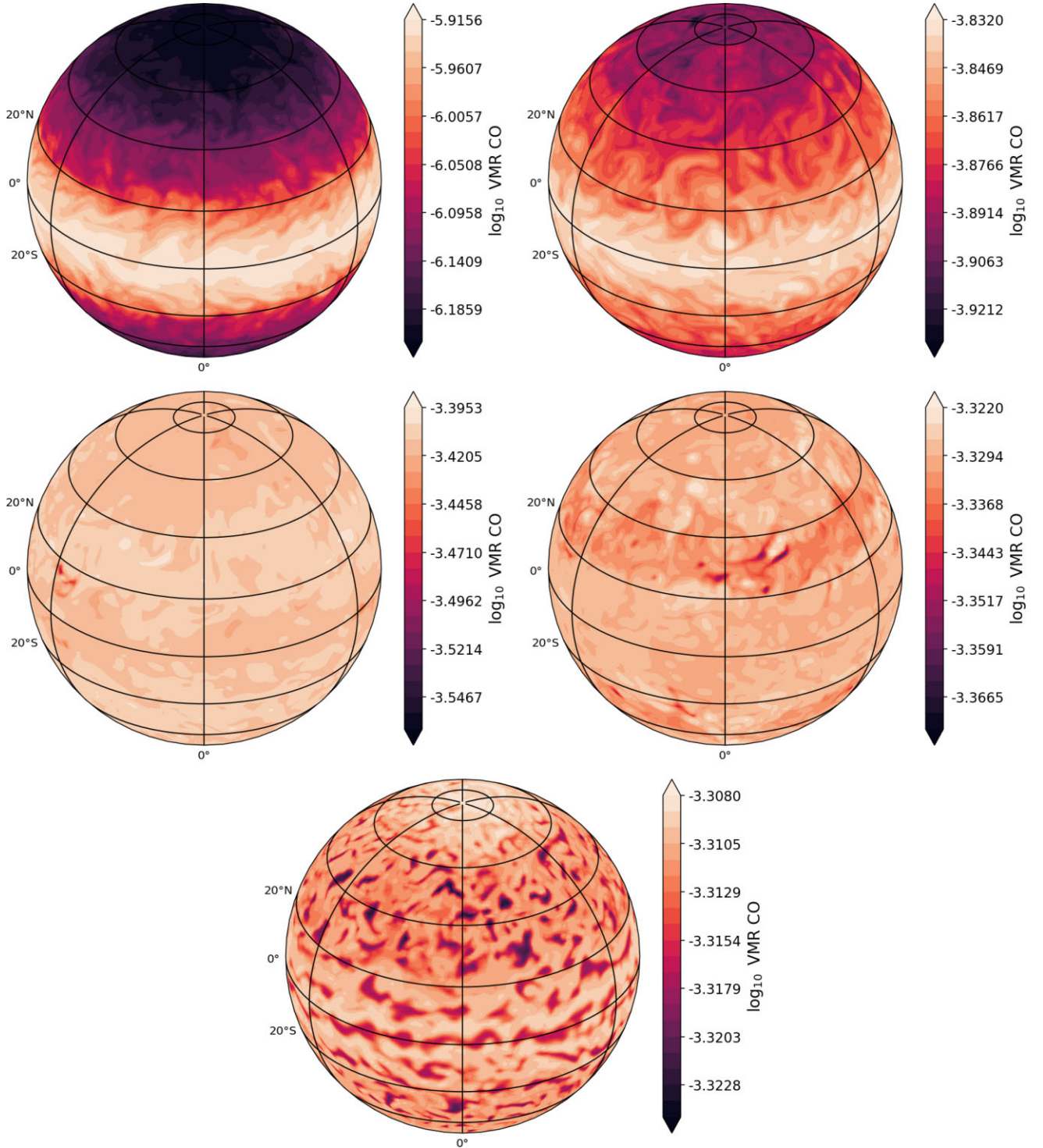


Figure 7. \log_{10} volume mixing ratio (VMR) of CO (colour bar) from each brown dwarf model at the end of the simulation at around a pressure level of 6 bar. $T_{\text{eff}} = 500$ (top left), 750 (top right), 1000 (middle left), 1250 (middle right), and 1500 K (bottom). Each simulation exhibits its spatial distribution of the species dependent on the dominant dynamical feature for each parameter regime. Storm regions at higher latitudes alter the VMR of CO over the course of a storm time-scale.

in the upper atmosphere, probably due again to the grey opacity assumption. Conversely, the Marley et al. (2021) models generally show a generally larger flux in the near-infrared regime, suggesting a slightly higher deeper temperature structure compared to our grey models. The Marley et al. (2021) models also include potassium in

the opacity mix, not included here, which is the primary opacity source responsible for the drop off in flux bluer than $\approx 1 \mu\text{m}$. The flux around this wavelength range from the GCM brown dwarf models is therefore likely overestimated from this lack of potassium absorption.

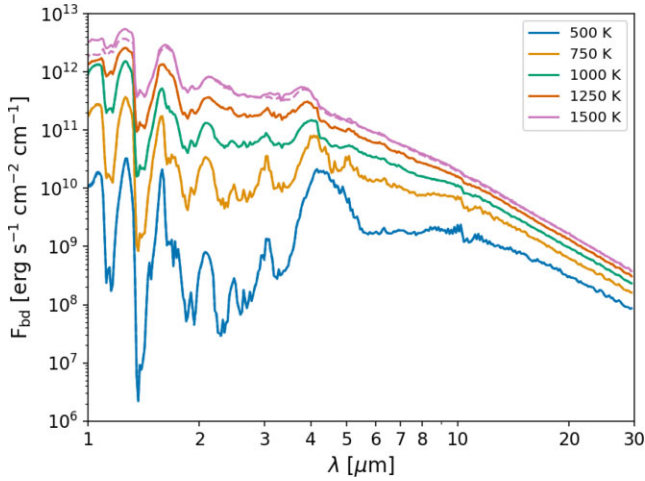


Figure 8. Emission spectra at the equator (solid lines) compared to the polar regions (dashed lines) for our different models. There is no appreciable difference in the spectra between the equator and pole regions in our simulations, apart from the hottest, $T_{\text{eff}} = 1500$ K, model.

8 DISCUSSION

There has been evidence suggesting that the near-infrared colour and variability amplitudes of brown dwarfs correlate with the viewing angles (e.g. Vos, Allers & Biller 2017; Vos et al. 2022). We have tested whether the horizontal variations of chemical species resulting from the 3D dynamics could significantly contribute to the viewing-angle-dependent spectrum, and we found that the effect is not significant (see Fig. 8). This is because the zonal-mean equator-to-pole variations of chemical species in our GCMs are small. But our current results do not exclude the role of chemically driven variations as a potential mechanism because our model does not include the radiative feedback of chemical species to the dynamics. Similar to the cloud-radiative-feedback dynamics (Tan & Showman 2021a,b), such a full dynamics–tracer-feedback coupling would be required to fully access potential mechanisms driving the large equator-to-pole differences, and we leave this as a next step.

There is an interesting transition in the zonal jet streams that the cooler models exhibit multiple alternating and weak jets, while the hotter models show fewer, broader, and stronger jets (see Fig. 1). Briefly speaking, the meridional width of the zonal jets forced by small-scale stochastic perturbations tend to follow the Rhines scale $L_\beta \sim \pi\sqrt{2U/\beta}$ (Rhines 1975), where U is the magnitude of the horizontal wind speed, $\beta = df/dy$ is the meridional gradient of f , and f is the Coriolis parameter. Given a rotation rate and a planetary radius, the stronger wind speeds in our hotter models naturally lead to broader and fewer jets than in the cooler models. Fig. 5 in Tan (2022) also nicely illustrates this jet behaviour. For a more in-depth discussion about the atmospheric dynamics under this forcing framework, readers are referred to our previous work of Showman et al. (2019) and Tan (2022). Then the question comes as to why hotter models have stronger wind speeds, and this is related to how strongly we apply the thermal perturbations (Tan 2022). The choices of our forcing amplitudes for each effective temperature are physically motivated that follows the scaling analysis in the appendix of Showman et al. (2019). At a given effective temperature, if one treats the forcing amplitude as a free parameter as in Tan (2022), the jets and the vertical mixing of chemical species would be stronger for higher forcing amplitudes. Lastly, the vertical mixing of chemical species is effectively done by the small-scale turbulent

motions rather than by the mean meridional motions associated with the jets (see the quantitative discussion in section 4.1 of Tan 2022). This is why in Figs 6 and 7, spatial distributions of chemical species show weak correlations to the zonal jets in Fig. 1 (i.e. strong chemical gradients are not cleanly delineated between the different zonal flow regions).

We have deliberately chosen not to include the formation of clouds as was done in previous similar models as they exhibit their own dynamical patterns and feedback mechanisms (e.g. Tan & Showman 2021a,b). In this study, we aim to isolate and understand the kinetic chemistry mechanisms without adding additional complex feedback from the presence of cloud coverage. Clouds alter the local thermodynamic properties of the atmosphere due to their strong opacity, which could go on to affect the chemical compositions through changes in local temperature and wind patterns. Our GCM also does not capture the mixing caused by small-scale gravity waves driven by localized convection, as seen in small-scale resolving models that include clouds (e.g. Freytag et al. 2010; Lefèvre et al. 2022). Our results could therefore be considered as a large-scale-driven ‘minimum mixing’ scenario in the stratospheric regions of brown dwarfs. Connecting the effect of clouds on the chemical kinetics will be an interesting prospect for future modelling efforts.

We assumed a simple grey opacity radiative transfer scheme to approximate the flux through the atmosphere. A more accurate method would be to use a spectral correlated- k opacity method as is common in hot Jupiter modelling efforts, however, this would further increase the computational burden by an order of magnitude or more, in particular since a higher GCM spatial resolution must be used in the brown dwarf models due to their faster rotation. Despite this, including MINI-CHEM, clouds, and a spectral radiative transfer to the base brown dwarf GCM model is a natural follow-on to this study. A possible avenue to explore is to apply faster correlated- k table mixing schemes such as adaptive equivalent extinction rather than random overlap (e.g. Amundsen et al. 2017). A further aspect of using a correlated- k scheme would be the inclusion of additional species that are optical wavelength absorbers such as Na, K, and FeH. These species’ opacity would also have to be mixed as well, possibly assuming their abundances at chemical equilibrium in the absence of a kinetic chemistry scheme for these species.

A wide variety of brown dwarf GCM parameters can be altered to explore dynamical structures across the expected brown dwarf parameter space. In this study, we focus on 10 h rotation rates with ‘middling’ bottom atmospheric drag, which is around the central values that were explored in Tan & Showman (2021b) and Tan (2022). This was chosen in order to elucidate the basic behaviour of the coupled MINI-CHEM GCM scheme in this atmospheric regime. Further studies that expand the parameter space will be highly interesting, however, we note that higher rotation rate atmospheres will require a higher GCM spatial resolution that would hinder the efficiency of the kinetic coupled scheme significantly.

We note that some species will quench at a higher pressure than the simulation boundary used in this study, this was seen in the Zahnle & Marley (2014) 1D models, where dependent on the parameter regime quenching could occur at pressures >100 bar, beyond the lower boundary of the GCM models. We note, however, that including deeper regions in the GCM will significantly increase the time for dynamical convergence of the GCM. Improvements to the kinetic chemical scheme to be more computationally efficient at higher pressures and temperatures will also be required to complete these simulations. This would be something to implement in future similar modelling efforts of this type in order to provide a more accurate quench level for species.

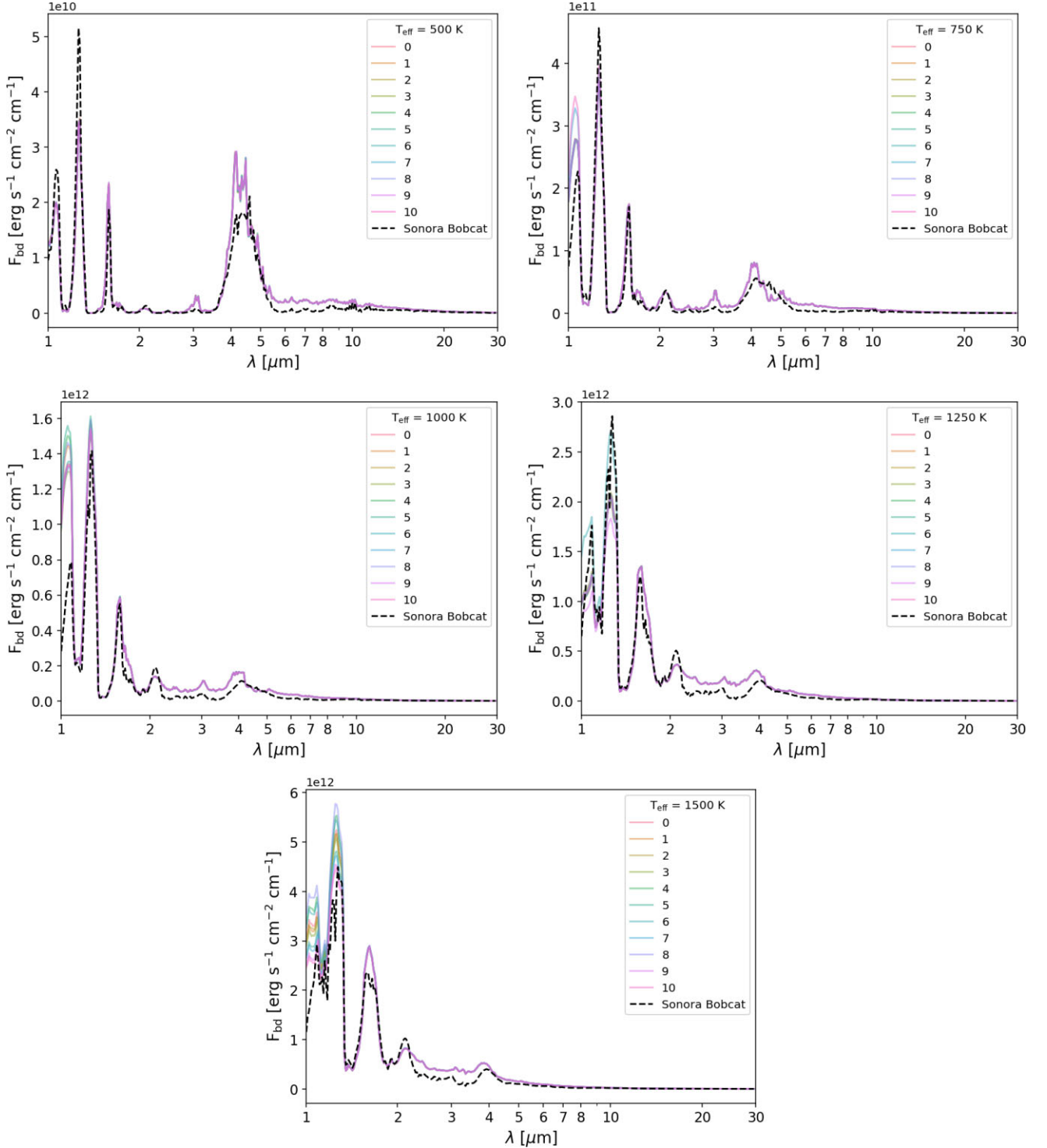


Figure 9. Emission spectra at the equator (coloured solid lines) of the brown dwarf simulations at hour intervals beyond the simulation end time for one rotation rate of 10 h. $T_{\text{eff}} = 500$ (top left), 750 (top right), 1000 (middle left), 1250 (middle right), and 1500 K (bottom). We compare to the equivalent Marley et al. (2021) Sonora Bobcat 1D radiative–convective equilibrium models (black dashed lines).

9 SUMMARY AND CONCLUSIONS

In this study, we explored a further small step in a holistic understanding of the dynamical features of brown dwarf atmospheres. We performed idealized 3D GCM models of a range of brown dwarf effective temperatures coupled to the miniature chemical kinetic

scheme MINI-CHEM in order to examine their 3D chemical structures. Our simulations show the rich spatial variations brought on by the interactions between the large-scale dynamical flows and small-scale atmospheric chemistry. We reproduce the strong non-equilibrium chemical signatures expected in brown dwarf atmospheres from

vertical mixing. Generally, species are well homogenized across the globe due to vertical and horizontal mixing of the atmosphere, with mixing ratio variations less than 10 per cent, dependent on the species. This is encouraging for 1D chemical kinetic models of brown dwarfs that concern the time- and global-mean state of the atmospheres. Tan (2022) provided analytic calculations of the mean vertical mixing coefficient, K_{zz} , under this forcing framework for chemical and cloud tracers and could be helpful for 1D models. This is further confirmed with the good agreement between the 1D VULCAN and global averaged GCM results presented in this study, which suggests 1D models may take advantage of GCM derived T - p and mixing profiles when characterizing these atmospheres.

Meanwhile, the development of storms and eddies in the atmosphere can produce localized regions of depletion or replenishment of chemical species at higher contrast to the background mean, sometimes up to 100 per cent. These storms form and dissipate dependent on the given storm time-scale and perturbation amplitudes in the brown dwarf simulations. In addition, similar to hot Jupiter studies, we find that the chemical structure of the atmosphere is inherently linked to the dynamical features of the brown dwarf atmosphere, with spatial variations of species following the wave patterns present in each simulation. This 3D effect is an important consideration when interpreting the time-resolved spectroscopic variability of brown dwarfs.

Spectra wise, little variation between equatorial and polar regions is seen and variability over the course of a rotational rate. Most variability is seen in the near-infrared wavelengths (1–1.5 μm), due to these wavelengths probing the thermal perturbation regions. This lack of variability is possibly due to our grey opacity assumption and cloud-free models. Including a cloud and correlated- k scheme able to take into account the changing spatial VMR of species produced by kinetics is a natural next step for these models.

Overall, our study elucidates further the complicated 3D coupling between chemistry and atmospheric dynamics for brown dwarf atmospheres. This study represents a useful stepping stone to the eventual performing of self-consistent 3D chemical modelling of these atmospheres in the future.

ACKNOWLEDGEMENTS

EKHL is supported by the SNSF Ambizione Fellowship grant (#193448). XT is supported by the European community through the ERC advanced grant EXOCONDENSE (PI: R. T. Pierrehumbert). S-MT is supported by the University of California, Riverside. The HPC support staff at AOPP, University of Oxford, and University of Bern is highly acknowledged.

DATA AVAILABILITY

The 1D radiative transfer, MINI-CHEM, and GCMCRT source codes are available on the lead author's GitHub: <https://github.com/ELeeAstro>. GCM output in NetCDF format and animated GIFs of Figs 2, 6, and 7 are available on Zenodo: <https://zenodo.org/record/7806376>. All other data are available upon request to the lead author.

REFERENCES

- Ackerman A. S., Marley M. S., 2001, *ApJ*, 556, 872
 Alderson L. et al., 2023, *Nature*, 614, 664
 Allard F., Hauschildt P. H., Alexander D. R., Tamanai A., Schweitzer A., 2001, *ApJ*, 556, 357

- Allard F., Homeier D., Freytag B., 2011, in Johns-Krull C. M., Browning M. K., West A. A., eds, ASP Conf. Ser. Vol. 448, 16th Cambridge Workshop on Cool Stars, Stellar Systems, and the Sun. Astron. Soc. Pac., San Francisco, p. 91
 Amundsen D. S., Tremblin P., Manners J., Baraffe I., Mayne N. J., 2017, *A&A*, 598, A97
 Apai D. et al., 2017, *Science*, 357, 683
 Barber R. J., Strange J. K., Hill C., Polyansky O. L., Mellau G. C., Yurchenko S. N., Tennyson J., 2014, *MNRAS*, 437, 1828
 Beltz H., Rauscher E., Roman M. T., Guiliat A., 2022, *AJ*, 163, 35
 Bordwell B., Brown B. P., Oishi J. S., 2018, *ApJ*, 854, 8
 Burgasser A. J. et al., 2002a, *ApJ*, 564, 421
 Burgasser A. J., Marley M. S., Ackerman A. S., Saumon D., Lodders K., Dahn C. C., Harris H. C., Kirkpatrick J. D., 2002b, *ApJ*, 571, L151
 Calamari E. et al., 2022, *ApJ*, 940, 164
 Carone L. et al., 2020, *MNRAS*, 496, 3582
 Chubb K. L., Tennyson J., Yurchenko S. N., 2020, *MNRAS*, 493, 1531
 Coles P. A., Yurchenko S. N., Tennyson J., 2019, *MNRAS*, 490, 4638
 de la Cruz Rodríguez J., Piskunov N., 2013, *ApJ*, 764, 33
 Drummond B. et al., 2020, *A&A*, 636, A68
 Fegley B., Jr, Lodders K., 1996, *ApJ*, 472, L37
 Freedman R. S., Lustig-Yaeger J., Fortney J. J., Lupu R. E., Marley M. S., Lodders K., 2014, *ApJS*, 214, 25
 Freytag B., Allard F., Ludwig H. G., Homeier D., Steffen M., 2010, *A&A*, 513, A19
 Geballe T. R., Saumon D., Golimowski D. A., Leggett S. K., Marley M. S., Noll K. S., 2009, *ApJ*, 695, 844
 Hammond M., Pierrehumbert R. T., 2017, *ApJ*, 849, 152
 Hargreaves R. J., Gordon I. E., Rey M., Nikitin A. V., Tyuterev V. G., Kochanov R. V., Rothman L. S., 2020, *ApJS*, 247, 55
 Harris G. J., Tennyson J., Kaminsky B. M., Pavlenko Y. V., Jones H. R. A., 2006, *MNRAS*, 367, 400
 Helling C., Casewell S., 2014, *A&AR*, 22, 80
 Helling C., Woitke P., Thi W. F., 2008, *A&A*, 485, 547
 Heng K., 2017, *Exoplanetary Atmospheres: Theoretical Concepts and Foundations*. Princeton Univ. Press, Princeton, NJ
 Hubeny I., Burrows A., 2007, *ApJ*, 669, 1248
 Innes H., Pierrehumbert R. T., 2022, *ApJ*, 927, 38
 Karalidi T., Marley M., Fortney J. J., Morley C., Saumon D., Lupu R., Visscher C., Freedman R., 2021, *ApJ*, 923, 269
 Karman T. et al., 2019, *Icarus*, 328, 160
 Komacek T. D., Showman A. P., 2016, *ApJ*, 821, 16
 Lacy B., Burrows A., 2023, *ApJ*, 950, 8
 Lee E. K. H., Casewell S. L., Chubb K. L., Hammond M., Tan X., Tsai S.-M., Pierrehumbert R. T., 2020, *MNRAS*, 496, 4674
 Lee E. K. H., Parmentier V., Hammond M., Grimm S. L., Kitzmann D., Tan X., Tsai S.-M., Pierrehumbert R. T., 2021, *MNRAS*, 506, 2695
 Lee E. K. H. et al., 2022, *ApJ*, 929, 180
 Lee E. K. H., Tsai S.-M., Hammond M., Tan X., 2023, *A&A*, 672, A110
 Lefèvre M., Tan X., Lee E. K. H., Pierrehumbert R. T., 2022, *ApJ*, 929, 153
 Leggett S. K. et al., 2021, *ApJ*, 918, 11
 Li G., Gordon I. E., Rothman L. S., Tan Y., Hu S.-M., Kass S., Campargue A., Medvedev E. S., 2015, *ApJS*, 216, 15
 Lian Y., Showman A. P., Tan X., Hu Y., 2022, *ApJ*, 928, 166
 Liu B., Showman A. P., 2013, *ApJ*, 770, 42
 Mang J., Gao P., Hood C. E., Fortney J. J., Batalha N., Yu X., de Pater I., 2022, *ApJ*, 927, 184
 Manjavacas E. et al., 2019, *ApJ*, 875, L15
 Marley M. S., Robinson T. D., 2015, *ARA&A*, 53, 279
 Marley M. S., Saumon D., Guillot T., Freedman R. S., Hubbard W. B., Burrows A., Lunine J. I., 1996, *Science*, 272, 1919
 Marley M. S., Seager S., Saumon D., Lodders K., Ackerman A. S., Freedman R. S., Fan X., 2002, *ApJ*, 568, 335
 Marley M. S. et al., 2021, *ApJ*, 920, 85
 Mayne N. J. et al., 2014, *A&A*, 561, A1
 Metchev S. A. et al., 2015, *ApJ*, 799, 154
 Miles B. E. et al., 2020, *AJ*, 160, 63
 Miles B. E. et al., 2023, *ApJ*, 946, L6

- Morley C. V., Fortney J. J., Marley M. S., Visscher C., Saumon D., Leggett S. K., 2012, *ApJ*, 756, 172
- Morley C. V., Marley M. S., Fortney J. J., Lupu R., Saumon D., Greene T., Lodders K., 2014, *ApJ*, 787, 78
- Morley C. V. et al., 2018, *ApJ*, 858, 97
- Mukherjee S., Fortney J. J., Batalha N. E., Karalidi T., Marley M. S., Visscher C., Miles B. E., Skemer A. J. I., 2022, *ApJ*, 938, 107
- Noll K. S., Geballe T. R., Marley M. S., 1997, *ApJ*, 489, L87
- Oppenheimer B. R., Kulkarni S. R., Matthews K., van Kerkwijk M. H., 1998, *ApJ*, 502, 932
- Phillips M. W. et al., 2020, *A&A*, 637, A38
- Polyansky O. L., Kyuberis A. A., Zobov N. F., Tennyson J., Yurchenko S. N., Lodi L., 2018, *MNRAS*, 480, 2597
- Prinn R. G., Barshay S. S., 1977, *Science*, 198, 1031
- Radigan J., Lafrenière D., Jayawardhana R., Artigau E., 2014, *ApJ*, 793, 75
- Reiners A., Basri G., 2008, *ApJ*, 684, 1390
- Rhines P. B., 1975, *J. Fluid Mech.*, 69, 417
- Rustamkulov Z. et al., 2023, *Nature*, 614, 659
- Saumon D., Geballe T. R., Leggett S. K., Marley M. S., Freedman R. S., Lodders K., Fegley B., Jr, Sengupta S. K., 2000, *ApJ*, 541, 374
- Saumon D., Marley M. S., Abel M., Frommhold L., Freedman R. S., 2012, *ApJ*, 750, 74
- Showman A. P., Tan X., Zhang X., 2019, *ApJ*, 883, 4
- Stephens D. C. et al., 2009, *ApJ*, 702, 154
- Tan X., 2022, *MNRAS*, 511, 4861
- Tan X., Showman A. P., 2021a, *MNRAS*, 502, 678
- Tan X., Showman A. P., 2021b, *MNRAS*, 502, 2198
- Tannock M. E. et al., 2021, *AJ*, 161, 224
- Tsai S.-M., Lyons J. R., Grosheintz L., Rimmer P. B., Kitzmann D., Heng K., 2017, *ApJS*, 228, 20
- Tsai S.-M., Malik M., Kitzmann D., Lyons J. R., Fateev A., Lee E., Heng K., 2021, *ApJ*, 923, 264
- Tsai S.-M., Lee E. K. H., Pierrehumbert R., 2022, *A&A*, 664, A82
- Tsai S.-M. et al., 2023, *Nature*, 617, 483
- Venot O., Bounaceur R., Dobrijevic M., Hébrard E., Cavalié T., Tremblin P., Drummond B., Charnay B., 2019, *A&A*, 624, A58
- Visscher C., Moses J. I., 2011, *ApJ*, 738, 72
- Vos J. M., Allers K. N., Biller B. A., 2017, *ApJ*, 842, 78
- Vos J. M., Faherty J. K., Gagné J., Marley M., Metchev S., Gizis J., Rice E. L., Cruz K., 2022, *ApJ*, 924, 68
- Witte S., Helling C., Hauschildt P. H., 2009, *A&A*, 506, 1367
- Yurchenko S. N., Mellor T. M., Freedman R. S., Tennyson J., 2020, *MNRAS*, 496, 5282
- Zahnle K. J., Marley M. S., 2014, *ApJ*, 797, 41
- Zamyatina M. et al., 2023, *MNRAS*, 519, 3129
- Zhang X., 2020, *Res. Astron. Astrophys.*, 20, 099

This paper has been typeset from a $\mathrm{T}_{\mathrm{E}}\mathrm{X}/\mathrm{L}^{\mathrm{A}}\mathrm{T}_{\mathrm{E}}\mathrm{X}$ file prepared by the author.